Theoretical and Applied Fracture Mechanics 124 (2023) 103794

Contents lists available at ScienceDirect

Theoretical and Applied Fracture Mechanics

journal homepage: www.elsevier.com/locate/tafmec

Hydrogen embrittlement of 2205 duplex stainless steel in *in-situ* tensile tests

V. Arniella *, G. Álvarez, J. Belzunce, C. Rodríguez

SIMUMECAMAT research group, University of Oviedo, E.P. Ingeniería, Campus universitario, 33203 Gijón, Spain

ARTICLE INFO

Keywords:
Hydrogen embrittlement
Duplex stainless steel
In-situ hydrogen charging tensile tests
Failure micromechanisms

ABSTRACT

Extensive use of hydrogen derived from renewable energy sources is currently limited by a lack of effective storage and transport solutions. Steels able to withstand hydrogen gas environments at high pressure are needed for the manufacture of safe and reliable storage vessels and pipes. The mechanical behavior of 2205 duplex stainless steel (54 % ferrite – 46 % austenite) was studied through tensile tests performed on smooth and notched specimens, submitted at the same time to electrochemical hydrogen charging. Hydrogen uptake was controlled by means of electrochemical charging and measured using a LECO DH603 hydrogen analyzer. The roles of different experimental parameters such as applied current density (from 0.02 to 0.5 mA/cm^2), electrolyte (1 M H_2SO_4 + As_2O_3 or 3 % NaCl solution), and applied displacement rate (from 0.002 to 0.4 mm/min) were also evaluated. Finally, the fracture surfaces of all the tested specimens were analyzed under a scanning electron microscope (SEM) and the prevalent failure micromechanisms were analysed.

Hydrogen embrittlement indexes in both smooth and notched specimens increase as hydrogen content in the electrolyte, current density increase and displacement rate decreases. In all the in-situ hydrogen charged tests, two different regions were observed in the fracture surfaces, a brittle region on the outer region of the specimen, enriched with hydrogen in the course of the test and a ductile region in the center of the specimen.

1. Introduction

The advent of hydrogen as a new energy vector requires the construction of new infrastructures that can transport and store it safely [1,2]. Hydrogen embrittlement (HE) has become a field of interest for many researchers in recent years [3–5]. It involves the entry of hydrogen atoms into the crystalline microstructure of steels, accumulating in locations where the embrittlement reaction takes place [6]. The diffusion and accumulation of hydrogen atoms in specific areas of the steel microstructure, such as grain boundaries and other internal interfaces, leads to a loss of mechanical properties, especially loss of ductility and toughness, causing the steel to fail under lower loads than in hydrogen-free environments [7,8].

The search for steel grades that efficiently resist hydrogen embrittlement is therefore a necessity. It is known that hydrogen embrittlement is produced when certain local hydrogen concentration and local stress (mechanical, thermal or residual) are attained in a susceptible microstructure. Under these conditions, critical combination of hydrogen concentration and local tensile stress are necessary for hydrogen embrittlement[6,9]. These determining factors for the initiation and propagation of cracks are well understood. However, the mechanisms by which failure occurs is still a matter of debate [10,11]. Among the main mechanisms proposed, the most commonly accepted are the following: hydrogen enhanced localized plasticity (HELP) [12–14], hydrogen enhanced decohesion (HEDE) [15,16], hydrogen adsorption induced by dislocation emission (AIDE) [17], and hydrogen-enhanced strain-induced vacancies (HESIV) [18].

Martensitic and ferritic stainless steels are very susceptible to hydrogen embrittlement. Many research works have evaluated HE in these steels [19–21]. In contrast, austenitic stainless steels are very resistant to HE, due in part to their very low hydrogen diffusion coefficient [22,23]. Several works on hydrogen embrittlement in these steels are also found in the literature [24–26]. The main drawbacks of austenitic stainless steels are their low yield strength and high cost, making them a poor choice for certain applications [27]. Duplex stainless steels (DSS), composed of roughly equal proportions of austenite and ferrite, were designed to improve the corrosion resistance already offered by austenitic steels and to provide products with higher strength, although the long-term mechanical performance of these steels in hydrogen rich environments is still not clear.

There are two types of tests to assess hydrogen embrittlement of steels. The first are ex-situ tests where specimens are hydrogen pre-

* Corresponding author.
E-mail address: arniellavictor@uniovi.es (V. Arniella).

https://doi.org/10.1016/j.tafmec.2023.103794
Received 2 November 2022; Received in revised form 18 January 2023; Accepted 26 January 2023
Available online 2 February 2023
0167-8442/© 2023 The Authors. Published by Elsevier Ltd. This is an open access article under the CC BY-NC-ND license (http://creativecommons.org/licenses/by-nc-nd/4.0/).

Table 1
Chemical composition of 2205 duplex stainless steel (% weight).

%C	%Mn	%Si	%P	%S	%Cr	%Ni
0.025	1.375	0.372	0.018	0.001	22.675	5.425
%Mo	**%N**	**%Nb**	**%V**	**%Ti**	**%Al**	**%Cu**
3.482	0.165	0.016	0.133	0.027	0.007	0.167

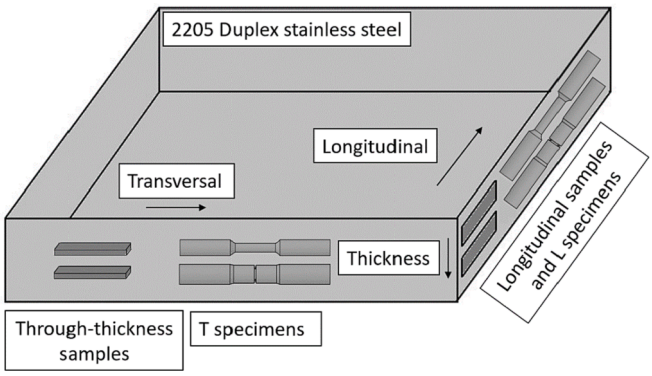

Fig. 1. Schematic representation of the samples taken from the steel plate.

charged either at high temperature and under pressure from hydrogen gas, or electrochemically from an aqueous solution. The second type of tests are in-situ hydrogen charging tests, where hydrogen charging occurs during mechanical loading.

The reaction of duplex stainless steels (DSS) to hydrogen has also been studied in recent years. Iacoviello et al. evaluated the mechanical

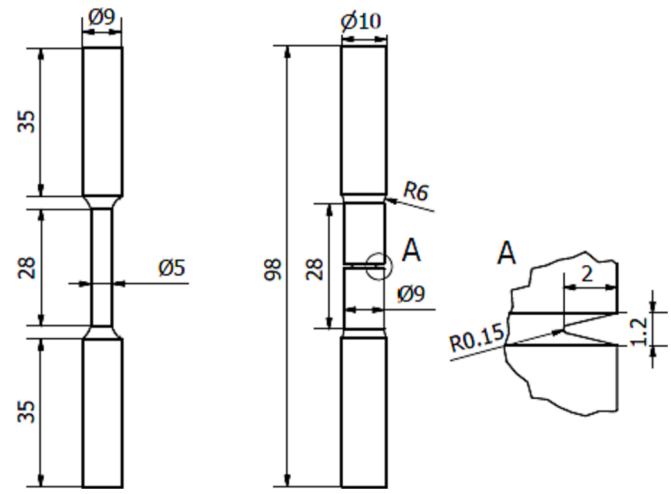

Fig. 3. Smooth and notched tensile specimen geometries (dimensions in mm).

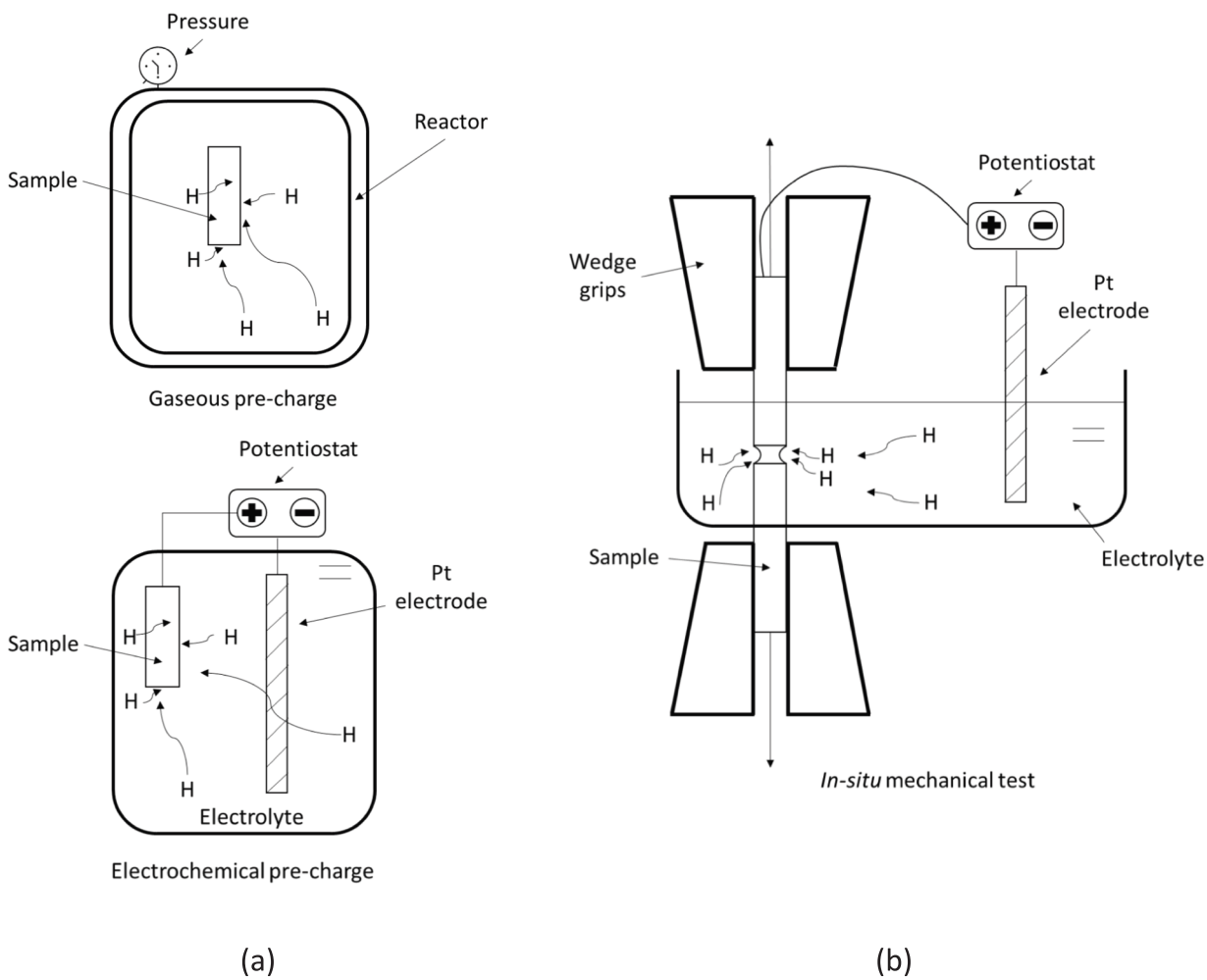

Fig. 2. (a) Gaseous and electrochemical hydrogen pre-charging (b) configuration to perform in-situ hydrogen charging tests (modified from [20]).

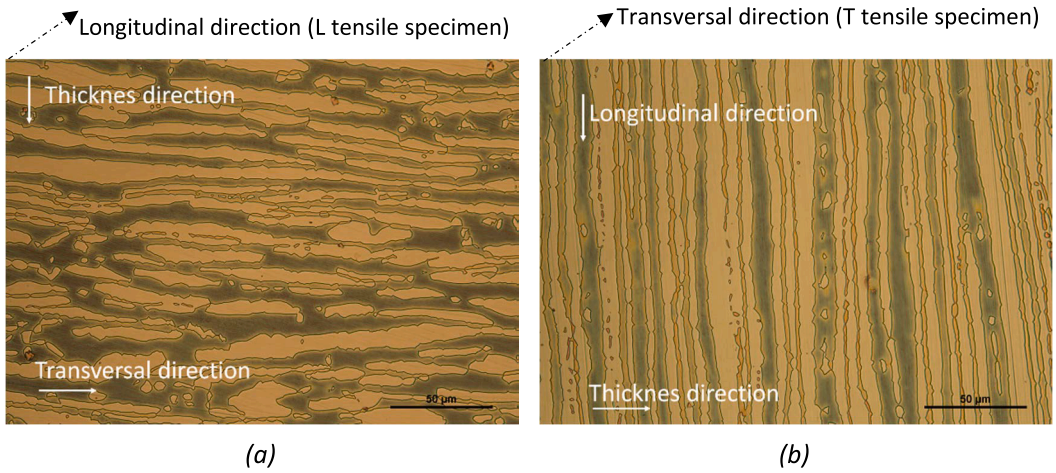

Fig. 4. 2205 optical micrographs, transversal sections of (a) longitudinal (L) tensile specimens (b) transversal (T) tensile specimens.

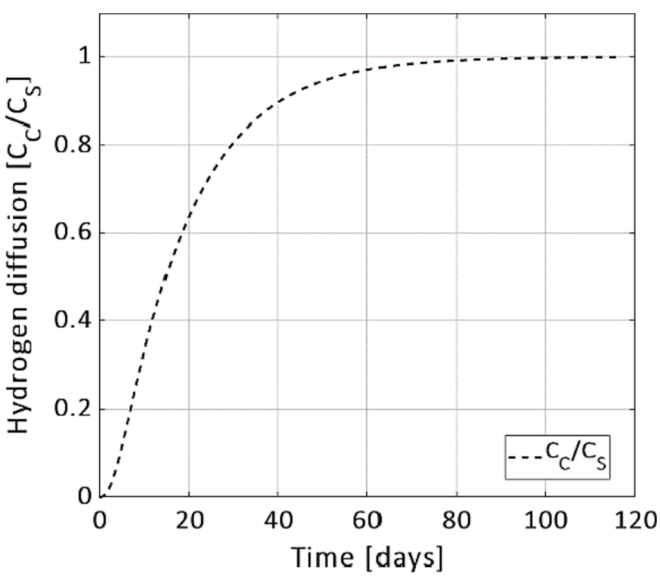

Fig. 5. Simulated diffusion results: ratio of mid-thickness and center hydrogen contents, C_C/C_S, versus time. 2205 steel sample with 1 mm thickness.

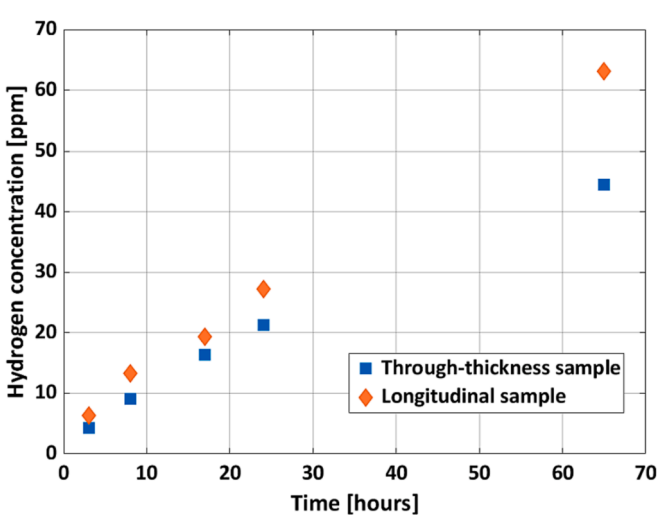

Fig. 6. Hydrogen content versus electrochemically charging time (acid solution under a current density of 0.50 mA/cm^2).

Table 2
Hydrogen content after electrochemical charging under different conditions for 24 h (through-thickness samples).

Ambient	Density current [mA/cm^2]	Hydrogen content [ppm]
1 M H_2SO_4 + 0.25 g/l As_2O_3	0.50	27.2
3 % NaCl	1.00	14.9
	0.10	6.8
	0.02	1.14
Hydrogen gas (190 bar, 40 °C)	–	1.14

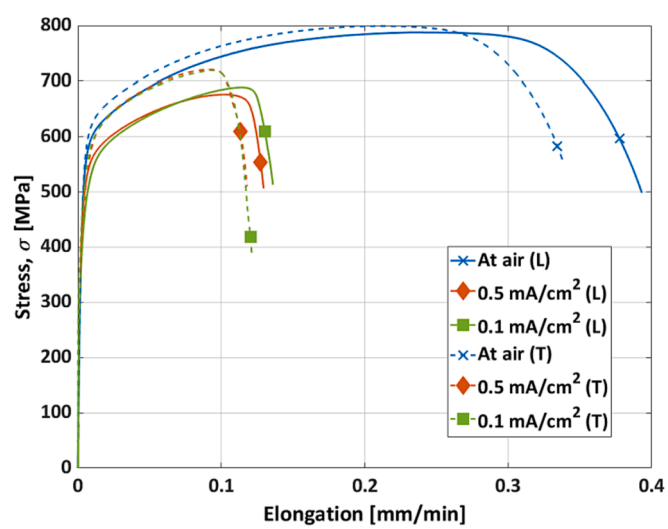

Fig. 7. Stress–strain curves corresponding to tensile tests performed on smooth specimens using the acid electrolyte under different current densities.

damage caused by hydrogen in a 2101 DSS [28] They performed low-strain-rate tensile tests after hydrogen pre-charging on different products submitted to different heat treatments. They found that 2101 DSS was prone to hydrogen embrittlement, reaching embrittlement ratios (related to elongation) of up to 80 % after specific heat treatments. Tao et al. studied the behavior of 2205 DSS after pre-strain hardening (from 0 to 20 %) [29]. The steel was pre-strained and then electrochemically hydrogen charged for 48 h prior to mechanical testing. In all cases, a loss of ductility was observed when the specimens were tested after

Table 3
Tensile test results (smooth specimens). In-situ hydrogen charged tests using the acid electrolyte (σ_{ys} is the yield strength, σ_u the ultimate tensile strength, e, the elongation and RA, the reduction of area and HEI their corresponding embrittlement indices).

Current density (mA/cm^2)	Displacement rate (mm/min)	Test time (min)	Specimen orientation	σ_{ys} (MPa)	σ_u (MPa)	$HEI_{\sigma u}$ (%)	e (%)	HEI_e (%)	RA (%)	HEI_{RA}(%)
In air	0.40	29	Longitudinal	524	787	–	39.5	–	70.1	–
		26	Transversal	533	797	–	33.1	–	56.5	–
			Average	528	792	–	36.3	–	63.3	–
0.10	0.01	485	Longitudinal	442	689	12	20.8	47	16.9	76
		485	Transversal	494	719	10	14.1	57	6.7	88
			Average	468	704	11	17.5	52	11.8	82
0.50	0.01	470	Longitudinal	470	676	14	20.0	49	22.0	69
		490	Transversal	490	721	10	16.7	50	4.2	93
			Average	480	699	12	18.4	50	13.1	81

Table 4
Tensile properties and corresponding embrittlement indexes (HEI) obtained with the in-situ hydrogen charging tests in saline electrolyte (longitudinal orientation).

Current density (mA/cm^2)	Displacement rate (mm/min)	Test time (min)	σ_{ys} (MPa)	σ_u (MPa)	$HEI_{\sigma u}$ (%)	e (%)	HEI_e (%)	RA (%)	HEI_{RA} (%)
In air	0.4	29	524	787	–	39.5	–	70.1	–
0.02	0.002	1135	484	736	7	39.4	0.3	58.1	17

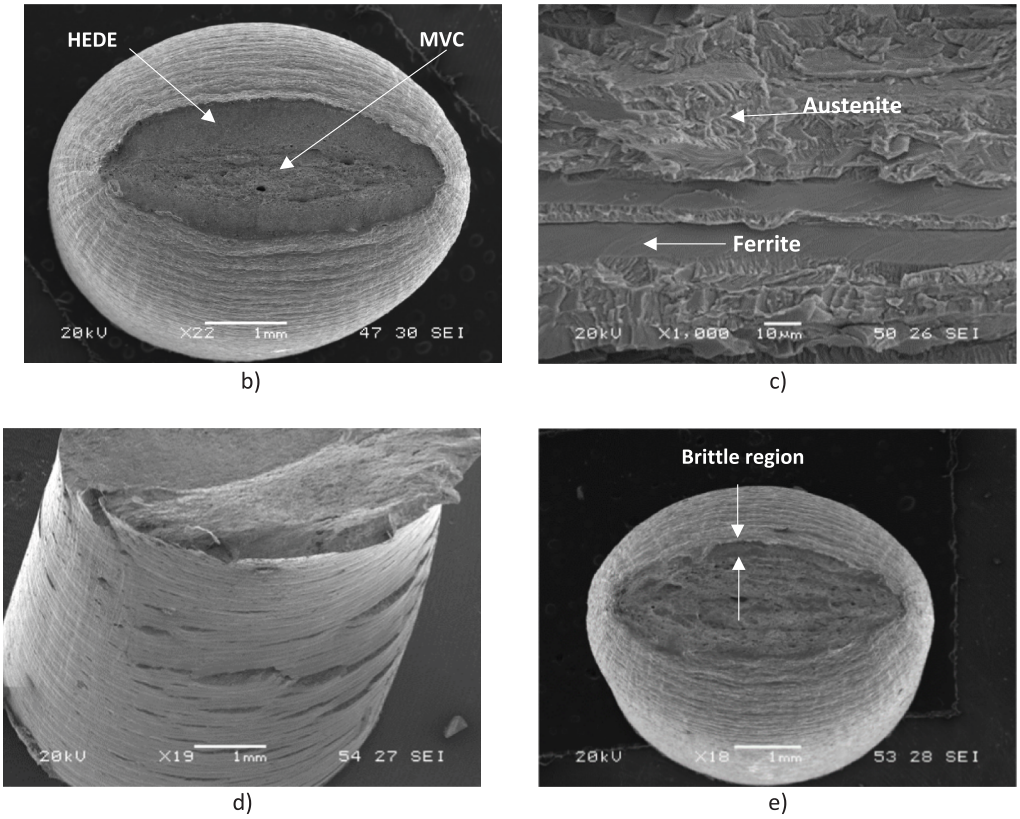

Fig. 8. a) Ductile failure (MVC) in a specimen tested in air, b) two regions with different operative failure micromechanisms (QC and MVC) in an specimen tested using the acid electrolyte, c) austenite and ferrite details in the peripheral region (QC failure micromechanism) of image b), d) microcracks observed in the calibrated length of the tensile specimen tested in acid electrolyte, e) failed section of specimen tested in saline electrolyte.

hydrogen pre-charging. According to the authors, the susceptibility to HE of this particular steel is due to the high diffusivity of hydrogen through the ferrite bands present in the microstructure of the steel as well as to the high hydrogen solubility in the austenite bands, where the critical hydrogen concentration that causes failure is reached very quickly. Similar conclusions were drawn by Okayasu and Fujiwara from their study, in which they compared an austenitic, a ferritic and a DSS steel [30]. They demonstrated through an exhaustive microstructural analysis using electron backscatter diffraction (EBSD) and scanning transmission electron microscopy (STEM) that hydrogen embrittlement damage in duplex steels occurs in the ferrite/austenite interface boundaries, but hardly ever in the ferrite or austenite bands themselves.

Despite all the work done on DSS, there is still a need to study its mechanical behavior in *in-situ* hydrogen charging tests: hydrogen enters differently when mechanical loads are applied during hydrogen charging, and surface plastic deformation also occurs. Ideally, *in-situ* hydrogen charging tests should be performed in a gaseous environment in order to simulate the service conditions of pressure vessels and pipes

Table 5
Tensile test parameters and embrittlement index (HEI) corresponding to in-situ hydrogen charging tests with acid electrolyte on notched specimens.

Current Density (mA/cm^2)	Displacement rate (mm/min)	Test time [min]	Specimen orientation	σ_{uN} (MPa)	$HEI_{\sigma uN}$ (%)	Embrittled depth (mm)
In air	0.400	7	Longitudinal	1370	–	–
		7	Transversal	1392	–	–
			Average	1381	–	–
0.10 mA/cm^2	0.010	207	Longitudinal	1214	11	0.43
		250	Transversal	1142	18	0.49
			Average	1178	15	0.46
	0.002	702	Longitudinal	930	32	0.70
		1247	Transversal	1084	22	0.53
			Average	1007	27	0.62
0.50 mA/cm^2	0.010	149	Longitudinal	1002	27	0.56
		181	Transversal	959	31	0.69
			Average	980	29	0.63
	0.002	689	Longitudinal	872	36	0.82

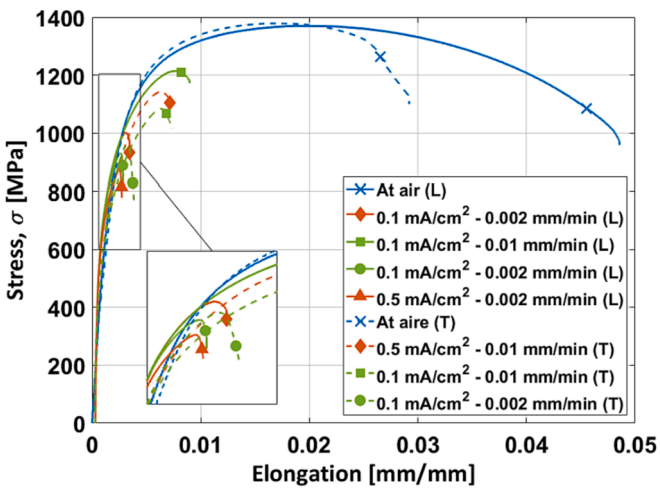

Fig. 9. Stress–strain curves of tensile test on notched specimens (acid electrolyte).

under hydrogen pressure, but the equipment required to perform these tests is costly and not always available. Electrochemical charging is a simpler and more economical way to perform these tests.

The aim of this work is to study the mechanical behavior of 2205 duplex stainless steel in hydrogen environments using smooth and notched tensile specimens. In order to study the influence of directionality caused by the austenite and ferrite bands in the steel microstructure, specimens extracted in both longitudinal and transversal directions were employed. In addition, tests were performed under *in-situ* hydrogen charging using different electrolytes, current densities and displacement rates.

2. Materials and methods

2.1. Steel

The material used in this study was 2205 duplex stainless steel supplied by Acerinox. Its chemical composition is shown in Table 1. A steel plate was hot-rolled, then annealed at 1080 °C, and finally water-cooled to obtain a final thickness of 10 mm.

2.2. Hydrogen charging

Two types of hydrogen charging samples were used on samples of 25x5x1 mm. The shortest dimension was parallel to the plate thickness direction for the through-thickness samples and parallel to the transversal direction for the longitudinal samples (Fig. 1). Before the charging process, the sample surfaces were polished and then washed with water and acetone to ensure better hydrogen ingress.

Five through-thickness samples were also pre-charged in a gaseous environment in a high pressure reactor, designed according to ASTM G146 [31]. According to the protocol, prior to hydrogen charging, an oxygen-free environment is ensured by applying several purges with an inert gas. A reasonable hydrogen charging time of 24 h under 190 bar and at 40 °C was set to simulate realistic operating conditions [32,33]. After charging, the reactor was de-pressurized, and the hydrogen pre-charged specimens were introduced in liquid nitrogen at −196 °C to limit hydrogen losses until hydrogen measurement [33].

Another batch of through-thickness samples as well as the longitudinal samples were hydrogen pre-charged under electrochemical conditions using two different electrolytes to achieve different hydrogen contents: an acid electrolyte based on a 1 M H_2SO_4 solution + 0.25 g/l of As_2O_3 and a 3 % NaCl saline solution. In addition, the applied current density was varied from 0.02 to 0.5 mA/cm^2. After charging for periods of time between 3 and 65 h, the hydrogen content was measured. At least two samples were analyzed for each condition. Fig. 2 a) shows schemes representing both hydrogen pre-charging methods.

2.3. Hydrogen content and hydrogen diffusion simulation

Thermal Desorption Analysis (TDA) was used to measure the hydrogen introduced in the hydrogenated samples. Hydrogen concentration was measured by means of a LECO DH603 hydrogen analyzer, able to measure hydrogen concentrations from 0.1 to 2500 ppm. In this work the sample was kept in the analyzer at 1100 °C for 300 s.

The introduction of hydrogen in the samples was also simulated through a simple unidirectional finite element analysis (FEA), implemented in an Abaqus commercial code, applying Fick's diffusion law, described in Equation (1)[34].

$$J = -D_{app}\nabla C_H \quad (1)$$

where D_{app} is the apparent hydrogen diffusion coefficient and C_H the hydrogen concentration. Finite element hydrogen diffusion analysis was performed on 25x5x1 mm plates using a hydrogen diffusion coefficient of $7.5{\cdot}10^{-14}$ m^2/s obtained by Iacoviello on similar steel [35]. A surface hydrogen concentration, C_S, was selected, assuming there was no hydrogen in the rest of the sample. The C_C/C_S ratio, between the amount of hydrogen present at the center of the sample, C_C, and that present at the surface, C_S, was calculated for different charging times. Saturation is attained when C_c/C_s is 1.

2.4. In-situ hydrogen charging tensile tests

In-situ hydrogen charging tensile tests were performed on both smooth and notched specimens in an Instron 5582, with a 100kN load cell.[36]. The geometries and dimensions of both types of specimens are shown in Fig. 3. The circumferential notch had a depth of 2 mm with a notch radius of 0.15 mm, giving rise to an elastic stress concentrator

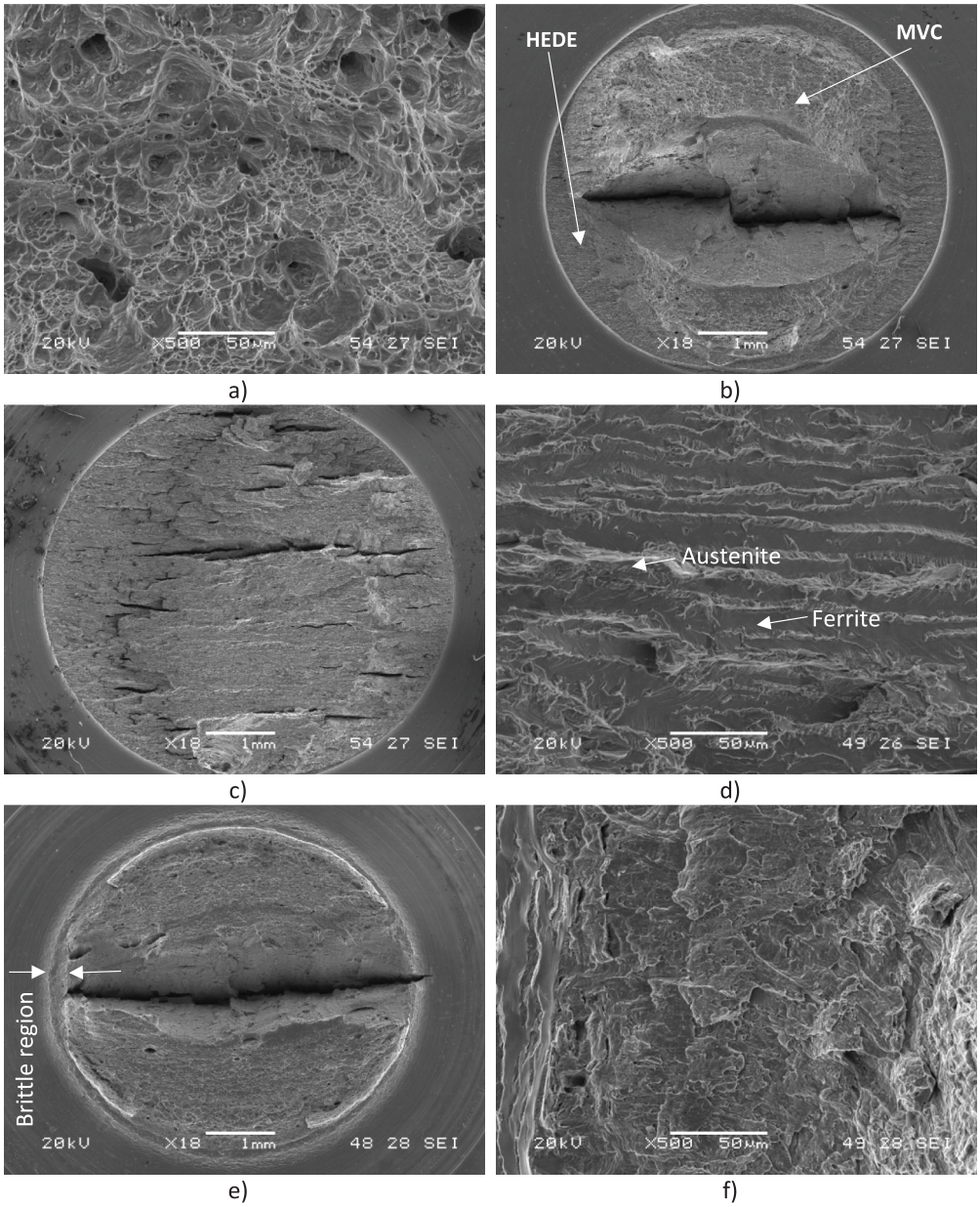

Fig. 10. Failed sections, a) specimen tested in air, b) tested under 0.10 mA/cm^2 and 0.010 mm/min (acid electrolyte), c) tested under 0.50 mA/cm^2 and 0.002 mm/min (acid electrolyte), d) failure detail in the peripheral region (QC) of image c), e) tested in the saline electrolyte, f) detail of the peripheral embrittled region observed in e).

Table 6
Notch tensile strength and embrittlement index (HEI) corresponding to in-situ hydrogen charging tests in the saline electrolyte (longitudinal sample).

Current Density (mA/cm^2)	Displacement rate (mm/min)	Test time (min)	σ_{uN} (MPa)	$HEI_{\sigma uN}$ (%)	Embrittled depth (mm)
At air	0.4	7	1370	–	–
0.02 mA/cm^2	0.002	1187	1251	9	0.1

factor of $k_t = 4.3$ [34]. Tensile specimens were extracted with their longitudinal axis parallel to both plate directions, transversal (T) and longitudinal (L). Their surfaces were polished and then washed first with water and then with acetone prior to starting the in-situ hydrogen charging tensile test.

Specimens of both smooth and notched geometries were first tested under laboratory conditions (in air) using a test displacement rate of 0.400 mm/min, according to the tensile test standard ISO 6892–1 [36]. For the in-situ hydrogen charging tensile tests, displacement rates between 0.002 and 0.010 mm/min were used to evaluate the influence of this parameter on hydrogen embrittlement. Two different current densities (0.50 and 0.10 mA/cm^2) were also evaluated, as well as the two electrolytes already mentioned (acid and saline). Fig. 2b) shows the arrangement used to perform these tests.

Hydrogen embrittlement was quantified by means of the hydrogen embrittlement index (HEI) given in Equation (2). The HEI varies from 0 % (no effect), to 100 % (maximum possible damage).

$$HEI[\%] = \frac{X - X_H}{X} \bullet 100 \quad (2)$$

where X and X_H are the steel tensile property evaluated in the absence of hydrogen and in the hydrogenated medium respectively. The HEI of the smooth specimens was calculated using tensile strength (σ_u),

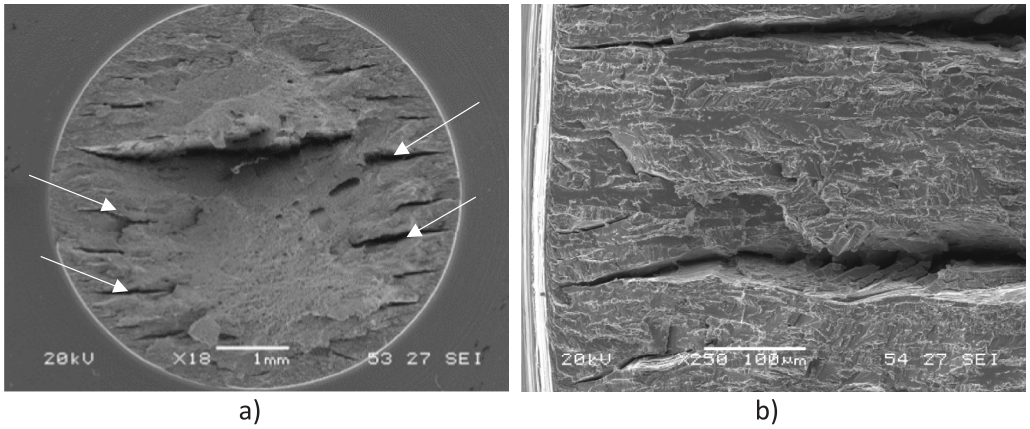

Fig. 11. a) Interlaminar cracks in the failed surface of a notched tensile test performed under 0.50 mA/cm^2 and 0.010 mm/min (acid electrolyte), b) detail of cracks.

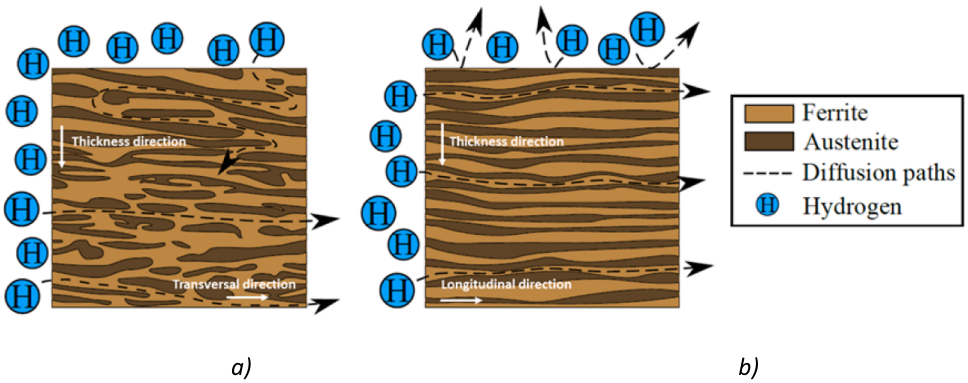

Fig. 12. Schematic hydrogen diffusion paths in transversal sections of (a) longitudinal (L) tensile specimens (b) transversal (T) tensile specimens.

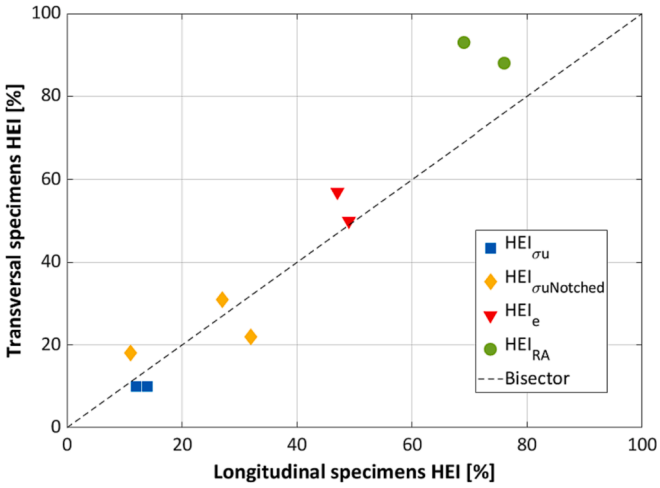

Fig. 13. Hydrogen embrittlement indexes corresponding to tensile tests carried out with longitudinal and transversal specimens.

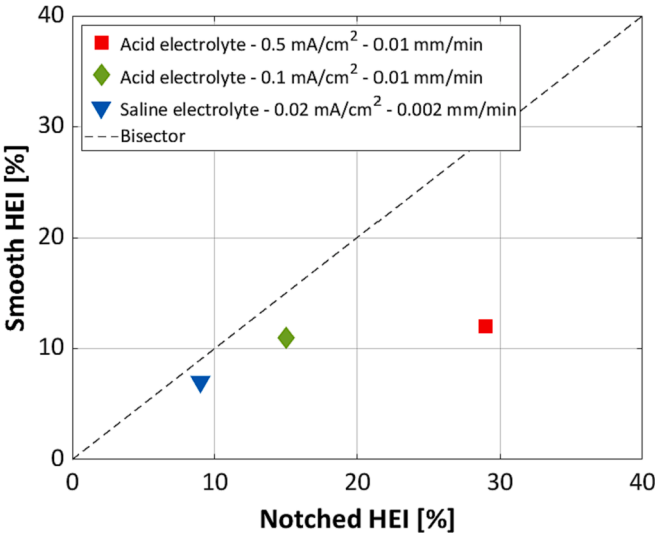

Fig. 14. Hydrogen embrittlement indexes relative to strength of tests performed with smooth and notched tensile specimens under different hydrogenated conditions.

elongation (e), and reduction of area (RA). For the notched specimens only notched tensile strength (σ_{uN}), defined as the maximum tensile load divided by the initial cross-sectional area of the notch region (5 mm diameter), was evaluated.

2.5. Microstructure and fracture surfaces

The microstructure of the steel was observed by optical microscopy with a Nikon Eclipse MA200, equipped with a software image analysis. The fracture surfaces of all the tested specimens were observed using a scanning electron microscope (SEM JEOL-JSM5600) under a voltage of 20 kV. The samples of the microstructural study were subjected to conventional metallographic preparation (grinding and polishing) and finally electrochemically etched using a reagent of 56 g KOH dissolved

in 100 ml of water under a voltage of 2 V for 3 s.

3. Results

3.1. Microstructure of 2205 duplex stainless steel

Fig. 4 shows the 2205 duplex steel microstructure observed in transversal sections of the longitudinal (L) and transversal (T) tensile specimens. The two phases constitutive of the steel, austenite (lighter phase) and ferrite (darker phase), are clearly differentiated. Volume fractions of 54 % of ferrite and 46 % of austenite were determined by manual point counting analysis. It is also worth noting that austenite and ferrite are stacked in the thickness direction, producing a banded microstructure. As hydrogen diffusion coefficient is orders of magnitude higher in ferrite than in austenite [37], it should be expected that most hydrogen will enter the steel through the ferrite bands.

3.2. Hydrogen saturation curves

Fig. 5 shows the diffusion curve obtained from the finite element analysis. The ratio between hydrogen content at mid-thickness (C_C) and in the sample surface (C_S) in 1 mm-thick samples of the 2205 steel against charging time is shown. As can be seen, more than 80 days are needed to attain homogeneous hydrogen distribution in these samples. This curve does not depend on the hydrogen content present on the sample surface, C_s, which is in equilibrium with the hydrogenated medium.

The evolution of hydrogen content with the exposure time measured using both through-thickness and longitudinal samples electrochemically pre-charged in a 1 M H_2SO_4 + 0.25 g/l of As_2O_3 solution under a density current of 0.50 mA/cm^2 are presented in Fig. 6. Measured hydrogen contents were always somewhat larger in the longitudinal samples and, as seen in Fig. 4, the hydrogen charged samples were always very far from saturation.

Table 2 shows hydrogen contents measured after 24 h of the through-thickness samples electrochemically charged under different conditions of current density. Table 2 also includes the hydrogen concentration measured when the same samples were charged in a pressure reactor at 190 bar of pure hydrogen at 40 °C for 24 h.

3.3. In-situ hydrogen charging tensile tests

3.3.1. Smooth tensile specimens

1 M H_2SO_4 + 0.25 g/l As_2O_3 electrolyte.

Results obtained from tests performed with smooth tensile specimens (L and T) *in-situ* hydrogen charged using the acid electrolyte are shown in Fig. 7. The tensile parameters obtained, the time spent on each kind of test and the embrittlement indexes corresponding to the tensile strength, elongation and the area reduction are also shown in Table 3. As can be seen, regardless of other test conditions, the results obtained are independent of the testing direction (longitudinal or transversal), so the average of both values in each condition are also reported in Table 3. Yield strength slightly decreases in these tests due to the entrance of hydrogen, denoting the action of a HELP mechanism. Hydrogen atoms enhanced local plasticity providing the start of dislocation movement under lower applied stresses.

Embrittlement indexes related to tensile strength are relatively low, just over 10 % (see also tensile curves presented in Fig. 7), but very high embrittlement indexes related to elongation and reduction of area were obtained, reaching values around 50 % and 80 % respectively. No significant embrittlement difference was observed when the applied current density was changed from 0.1 to 0.5 mA/cm^2.

3 % NaCl electrolyte.

A current density of 0.02 mA/cm^2 was selected to provide a hydrogenation medium similar to a hydrogen pressure of 190 bar at 40 °C (see Table 2). A hydrogen content of 1.14 ppm was achieved in 24 h under both conditions. The results obtained in the tests with the smooth tensile specimens are shown in Table 4.

The hydrogen embrittlement indexes in these tests were much lower than those carried out with the acid electrolyte, with a small reduction of yield stress and more significant ultimate tensile strength (7 %) and reduction of area embrittlements (17 %).

3.3.1.1. Failure analysis. In order to identify the operative failure micromechanisms, all the failed sections were observed under the scanning electron microscope (SEM). The operative failure micromechanism was fully ductile, characterized by microvoid coalescence (MVC), in all tests performed in air, Fig. 8 a). Nevertheless, in both in-situ hydrogen charging tests, using the acid electrolyte and the saline solution, two operative failure micromechanisms were always observed; MVC in the center of the specimens, and a brittle failure in the peripheral region, where hydrogen accumulates during the test (Fig. 8b). The failure micromechanism operative in the peripheral brittle region corresponds to quasi-cleavage, QC, characterized by flat cleavage facets in the ferrite and a rougher surface, denoting the existence of local plasticity in the austenite [11,38,39] (Fig. 8c). In addition, small cracks were found in the calibrated section of the tensile specimen (Fig. 8d), which may be due to strong hydrogen accumulations in the specimen surface, especially at the austenite-ferrite interfaces. On the other hand, the brittle regions observed in tests with the saline electrolyte at a current density of 0.02 mA/cm^2 were significantly smaller due to the lower hydrogen activity of this medium (Table 2) and embrittlement susceptibility (Fig. 8e).

3.3.2. Notched specimens

1 M H_2SO_4 + 0.25 g/L As_2O_3 electrolyte.

The notch strengths and corresponding embrittlement factors obtained in these tests are presented in Table 5. The embrittled depth (depth of the brittle region) measured under the scanning electron microscope is also shown in Table 5. It corresponds to the maximum hydrogen diffusion depth in the in-situ hydrogen charging test.

As with the smooth tensile specimens, similar results were obtained in both longitudinal and transversal directions. The average values are also given in Table 5. Hydrogen embrittlement indexes and embrittlement depths increase as current density increases because of the higher hydrogen activity provided by the electrolytic medium. In addition, when the displacement rate decreases, there is a longer time for hydrogen diffusion and accumulation, embrittlement indexes increase and larger embrittled depth is observed. An average embrittlement index of 36 % was obtained in the tests performed under the highest current density (0.5 mA/cm^2) and the lowest displacement rate (0.002 mm/min). Characteristic stress–strain curves obtained in these tests are shown in Fig. 9. A significant decrease in total elongation when the current density increases or the test rate decreases is also clear; the reduction of area measured in all these specimens was near zero.

3 % NaCl electrolyte.

As in the case of the smooth tensile specimens, hydrogen embrittlement of notched specimens tested in the saline electrolyte was quite low: only 9 % under a low displacement rate of 0.002 mm/min. Nevertheless low but visible embrittled depth was measured (0.1 mm).

3.3.2.1. Failure analysis. The failure micromechanism found in all tests performed in air was fully ductile, MVC (Fig. 10a). In contrast, two different failed regions were always present in tests performed under *in-situ* hydrogen charging (Fig. 10 b), c), e)): a brittle peripheral region where QC was the only operative micromechanism (Fig. 10 d), f)) and a central ductile region characterized by microvoids coalescence, MVC. The extension of both regions depends on the hydrogen activity of the medium, that is the type of electrolyte and current density, as well as on the applied displacement rate (see embrittlement depths in Tables 5 and 6).

4. Discussion

It was confirmed that as reported in [37–39], hot rolled duplex 2205 stainless steels are susceptible to hydrogen embrittlement and that microstructure plays an important role in HE. Hot rolled 2205 duplex stainless steel is composed of austenite blocks (face centered cubic, FCC, γ phase) aligned in the thickness direction dispersed on a ferrite matrix (body centered cubic, BCC, α phase), as shown in Fig. 3. According to several studies, hydrogen diffusivity is 10^4-10^5 times higher in ferrite than in austenite, while hydrogen solubility is 2–3 orders of magnitude higher in austenite [32,37,40]. In the microstructure of 2205 duplex steel, most hydrogen enters and diffuses into the steel microstructure through the ferrite bands and accumulates in the ferrite–austenite interfaces. Wu et al. [41] have demonstrated using hydrogen microprinting (HMT) and also in-situ scanning Kelvin probe force microscopy (SKPFM) techniques that austenite-ferrite interfaces are the main hydrogen traps in duplex stainless steels and different authors [42,43] have also shown that hydrogen cracks extended preferably through such phase boundaries. This may explain the presence of inter-laminar cracks, shown in Fig. 11.

Fig. 12 shows the diffusion of hydrogen in the 2205 duplex microstructure corresponding to the longitudinal (Fig. 11.a) and transversal (Fig. 11.b) sections of tensile specimens. Most hydrogen diffuses through the ferrite bands as austenite blocks are effective barriers to the movement of hydrogen atoms. Thus, hydrogen has a similar effect on longitudinal and transversal tensile specimens: only a more tortuous hydrogen path and consequently a slower hydrogen diffusion would be expected in the through-thickness steel direction. This also explains the lower hydrogen contents measured in the T samples shown in Fig. 5. In fact, the permeation experiments of Wu et al. [41] identified a significantly lower diffusion coefficient in the thickness direction than in the longitudinal direction in 2205 duplex stainless steel.

The hydrogen embrittlement similarity observed between longitudinal and transversal tensile specimens is better seen in Fig. 13, where embrittlement indexes obtained in tests performed with the acid electrolyte on smooth and notched tensile specimens of both orientations are plotted together. With the exception of the embrittlement indexes referring to the reduction in area measured with smooth tensile specimens, the results obtained in both orientations are similar. The effect of specimen orientation on this particular hydrogen embrittlement index is undoubtedly related to the oval failed section always observed in these tests (see Fig. 8 b, c), in which the shortest axis of the ellipse corresponds to the thickness of the plate.

Embrittlement indexes related to the strength obtained with smooth and notched specimens are plotted together in Fig. 14. HEIs obtained using notched specimens are always higher and this difference is accentuated as the hydrogen activity of the hydrogenating medium increases.

According to Oriani's theory [44], hydrogen accumulates in the region of the specimen submitted to the highest hydrostatic stress, with local hydrogen concentration in this region reaching larger values under higher hydrostatic stresses. Hydrostatic stresses are always larger in the notched tensile test specimens and, consequently, the largest hydrogen accumulations and embrittlement are expected in these cases. Moreover, in all the *in-situ* hydrogen charging tensile tests, hydrogen enters into the specimens when its surface is been submitted to plastic deformation. Then, hydrogen in equilibrium with the hydrogenating medium largely increases due to this reason and local plastic deformation is much larger in notched specimens due to the stress concentration.

5. Conclusions

The effect of hydrogen on 2205 duplex stainless steel using in-situ hydrogen charging tensile tests is analyzed in this work. The main conclusions are the following:

- Embrittlement indexes in both smooth and notched tensile specimens increase when hydrogen activity of the electrolytic medium increases and when the displacement rate decreases.
- Yield stress and tensile strength suffer small decreases with the entrance of hydrogen, however, properties related with ductility such as elongation and reduction of area, were more affected.
- Two differentiated failed regions were observed on the failed surfaces of the in-situ hydrogen charging samples, a peripheral region characterized by a brittle quasi-cleavage micromechanism and a central ductile zone, characterized by microvoid coalescence (MVC).
- The acid electrolyte caused higher embrittlement indexes, due to higher hydrogen activity. However, using the saline electrolyte, a more realistic hydrogenation condition similar to high pressure hydrogen gas (190 bar) was achieved.
- The presence of a stress concentrator (notch) accentuates hydrogen embrittlement, as hydrogen accumulates in the region of high triaxiality present in front of the notch tip.
- Hydrogen enters quickly through the ferrite bands, as its hydrogen diffusion coefficient is much higher than in austenite, and accumulates in the ferrite–austenite interfaces, leading to interface cracking.

Declaration of Competing Interest

The authors declare that they have no known competing financial interests or personal relationships that could have appeared to influence the work reported in this paper.

Data availability

Data will be made available on request.

Acknowledgements

To the Spanish Ministry of Science, Innovation and Universities for the financial support received through RTI2018-096070-B-C31 and PID2021-124768OB-C22 research projects and the Victor Arniella FPI grant PRE2019-088533. To the Principality of Asturias for the AYUD-2021-50985 and G. Alvarez Severo Ochoa grant PA-20-PF-BP19-087. To the Scientific-Technical Services of the University of Oviedo for the use of the SEM JEOL-JSM5600 scanning electron microscope.

References

[1] Hydrogen Roadmap Europe Report, 2019. https://doi.org/10.2843/249013.
[2] A. Martin, M.F. Agnoletti, E. Brangier, Users in the design of Hydrogen Energy Systems: A systematic review, Int. J. Hydrogen Energy. 45 (2020) 11889–11900, https://doi.org/10.1016/j.ijhydene.2020.02.163.
[3] L. Dong, S. Wang, G. Wu, et al., Application of atomic simulation for studyin hydrogen embrittlement phenomena and mechanism in iron-based alloys, Int. J. Hydrogen Energy 47 (2022) 20288–20309, https://doi.org/10.1016/j.ijhydene.2022.04.119.
[4] H. Wang, X. Cheng, Y.G. Zhang, M.M. Wang, B.L. Zhao, Z.M. Xie, T. Zhang, R. Liu, X.B. Wu, X.P. Wang, Q.F. Fang, C.A. Chen, C.S. Liu, Hydrogen embrittlement of bulk W-0.5 wt% ZrC alloy induced by annealing in hydrogen atmosphere, J. Nucl. Mater. 556 (2021) 153177.
[5] B.C.E. Schibicheski Kurelo, G.B. de Souza, F.C. Serbena, C.M. Lepienski, R. F. Chuproski, P.C. Borges, Improved saline corrosion and hydrogen embrittlement resistances of superaustenitic stainless steel by PIII nitriding, J. Mater. Res. Technol. 18 (2022) 1717–1731.
[6] A. Mohammadi, P. Edalati, M. Arita, J.W. Bae, H.S. Kim, K. Edalati, Microstructure and defect effects on strength and hydrogen embrittlement of high-entropy alloy CrMnFeCoNi processed by high-pressure torsion, Mater. Sci. Eng. A 844 (2022) 143179.
[7] J.P. Hirth, Effects of Hydrogen on the Properties of Iron and Steel, Metall. Mater. Trans. 11 (6) (1980) 861–890.
[8] R. Singh, V. Singh, A. Arora, D.K. Mahajan, In-situ investigations of hydrogen in fl uenced crack initiation and propagation under tensile and low cycle fatigue loadings in RPV steel, J. Nucl. Mater. 529 (2020), 151912, https://doi.org/10.1016/j.jnucmat.2019.151912.
[9] B.N. Popov, J. Lee, M.B. Djukic, H. Permeation, H.-I. Cracking, Third Edit, Elsevier Inc., 2018, 10.1016/B978-0-323-52472-8.00007-1.
[10] X. Li, X. Ma, J. Zhang, E. Akiyama, Y. Wang, X. Song, Review of hydrogen embrittlement in metals: Hydrogen diffusion, hydrogen characterization, hydrogen

embrittlement mechanism and prevention, Acta Metall. Sin. (English Lett.) 33 (6) (2020) 759–773.
[11] M. Wasim, M.B. Djukic, T.D. Ngo, Influence of hydrogen-enhanced plasticity and decohesion mechanisms of hydrogen embrittlement on the fracture resistance of steel, Eng. Fail. Anal. 123 (2021), 105312, https://doi.org/10.1016/j.engfailanal.2021.105312.
[12] H.K. Birnbaum, P. Sofronis, Hydrogen-enhanced localized plasticity–a mechanism for hydrogen- related fracture, Mater. Sci. Eng 176 (1-2) (1994) 191–202.
[13] H.K. Birnbaum, Mechanisms of hydrogen related fracture of metals, (1989).
[14] Y. Jagodzinski, H. Hänninen, O. Tarasenko, S. Smuk, Interaction of hydrogen with dislocation pile-ups and hydrogen induced softening of pure iron, Scr. Mater. 43 (2000) 245–251, https://doi.org/10.1016/S1359-6462(00)00398-5.
[15] L.B. Pfeil, The Effect of Occluded Hydrogen on the Tensile Strength of Iron (1926) 182–195, https://doi.org/10.1098/rspa.1926.0103.
[16] Z. Tarzimoghadam, M. Rohwerder, S.V. Merzlikin, A. Bashir, L. Yedra, S. Eswara, Acta Materialia Multi-scale and spatially resolved hydrogen mapping in a Ni e Nb model alloy reveals the role of the d phase in hydrogen embrittlement of alloy 718, Acta Mater. 109 (2016) 69–81, https://doi.org/10.1016/j.actamat.2016.02.053.
[17] S.P. Lynch, Environmentally assisted cracking: Overview of evidence for and adsorption-induced localised-slip process, Acta Metall. 36 (1988) 2639–2661, https://doi.org/10.1016/0001-6160(88)90113-7.
[18] M. Nagumo, Hydrogen related failure of steels – a new aspect, Materials Science and Technology 20 (8) (2004) 940–950.
[19] A. Zafra, L.B. Peral, J. Belzunce, Hydrogen diffusion and trapping in A 42CrMo4 quenched and tempered steel: Influence of tempering temperature, Int. J. Hydrogen Energy. 43 (2020) 31225–31242, https://doi.org/10.1016/j.ijhydene.2020.08.134.
[20] V. Arniella, A. Zafra, G. Álvarez, J. Belzunce, C. Rodríguez, Comparative study of embrittlement of quenched and tempered steels in hydrogen environments, Int. J. Hydrogen Energy 47 (38) (2022) 17056–17068.
[21] A. Zafra, Study on Hydrogen Diffusivity and Embrittlement of Quenched and Tempered 42CrMo4 Steel, 2021.
[22] A. Turnbull, Hydrogen diffusion and trapping in metals, Woodhead Publishing Limited (2012), https://doi.org/10.1533/9780857095374.1.89.
[23] M. Alexander Stopher, P.E.J. Rivera-Diaz-del-Castillo, Hydrogen embrittlement in bearing steels, Hydrogen embrittlement in bearing steels 32 (11) (2016) 1184–1193.
[24] H.-J. Cho, Y. Cho, H. Gwon, S. Lee, S.S. Sohn, S.-J. Kim, Effects of Ni/Cu replacement on improvement of tensile and hydrogen-embrittlement properties in austenitic stainless steels, Acta Mater. 235 (2022) 118093.
[25] Y.i. Luo, W. Li, L. Jiang, N. Zhong, X. Jin, Hydrogen embrittlement and hydrogen diffusion behavior in interstitial nitrogen-alloyed austenitic steel, Int. J. Hydrogen Energy 46 (64) (2021) 32710–32722.
[26] S.-G. Kim, S.-H. Shin, B. Hwang, Machine learning approach for prediction of hydrogen environment embrittlement in austenitic steels, J. Mater. Res. Technol. 19 (2022) 2794–2798, https://doi.org/10.1016/j.jmrt.2022.06.046.
[27] J. Yamabe, T. Awane, S. Matsuoka, Investigation of hydrogen transport behavior of various low-alloy steels with high-pressure hydrogen gas, Int. J. Hydrogen Energy. 40 (2015) 11075–11086, https://doi.org/10.1016/j.ijhydene.2015.07.006.
[28] F. Iacoviello, V. Di Cocco, C. Bellini, L. Sorrentino, Hydrogen embrittlement in a 2101 lean duplex stainless steel, Procedia Struct. Integr. 18 (2019) 391–398, https://doi.org/10.1016/j.prostr.2019.08.180.
[29] P. Tao, F. Ye, W. Cen, J. Zhao, Y. Wang, J. Gong, Analysis of enhanced hydrogen embrittlement fracture for pre-strain hardening 2205 duplex stainless steel, Results Phys. 16 (2020) 102820.
[30] M. Okayasu, T. Fujiwara, Effects of microstructural characteristics on the hydrogen embrittlement characteristics of austenitic, ferritic, and γ–α duplex stainless steels, Mater. Sci. Eng. A 807 (2021) 140851.
[31] Astm, Standard Practice for Evaluation of Disbonding of Bimetallic Stainless Alloy / Steel Plate for Use in High-Pressure, High-Temperature Refinery, Cell. 01 (2001) 1–6, https://doi.org/10.1520/G0146-01R13.1.
[32] C.S. Marchi, B.P. Somerday, S.L. Robinson, Permeability, solubility and diffusivity of hydrogen isotopes in stainless steels at high gas pressures, Int. J. Hydrogen Energy 32 (2007) 100–116, https://doi.org/10.1016/j.ijhydene.2006.05.008.
[33] The American Society of Mechanical Engineers, ASME B31.12 - Hydrogen Piping and Pipelines, Asme Int. 2011, 1-272 (2014).
[34] A. Zafra, L.B. Peral, J. Belzunce, C. Rodríguez, Effect of hydrogen on the tensile properties of 42CrMo4 steel quenched and tempered at different temperatures, Int. J. Hydrogen Energy. 43 (2018) 9068–9082, https://doi.org/10.1016/j.ijhydene.2018.03.158.
[35] F. Iacoviello, J. Galland, M. Habashi, A thermal outgassing method (T.O.M.) to measure the hydrogen diffusion coefficients in austenitic, austeno-ferritic and ferritic-perlitic steels, Corros. Sci. 40 (1998) 1281–1293, https://doi.org/10.1016/S0010-938X(97)00145-5.
[36] UNE-EN ISO 6892-1, Metallic Materials. Tensile testing. Part 1: Method of test at room temperature. (2019).
[37] A. Turnbull, R.B. Hutchings, Analysis of hydrogen atom transport in a two-phase alloy, Mater. Sci. Eng. A 177 (1994) 161–171, https://doi.org/10.1016/0921-5093(94)90488-X.
[38] T. Wang, H. Zhang, W. Liang, Hydrogen embrittlement fracture mechanism of 430 ferritic stainless steel: The significant role of carbides and dislocations, Mater. Sci. Eng. A 829 (2022), 142043, https://doi.org/10.1016/j.msea.2021.142043.
[39] L.B. Peral, A. Díaz, V. Arniella, J. Belzunce, J. Alegre, I.I. Cuesta, Hydraulic fracture behavior in the presence of hydrogen in notched miniature cylindrical specimens of a 42CrMo4 steel, Eng. Fract. Mech. 274 (2022) 108749.
[40] K. Kiuchi, R.B. McLellan, The solubility and diffusivity of hydrogen in well-annealed and deformed iron, Acta Metall. 31 (7) (1983) 961–984.
[41] W. Wu, X. Zhang, W. Li, H. Fu, S. Liu, Y. Wang, J. Li, Effect of hydrogen trapping on hydrogen permeation in a 2205 duplex stainless steel: Role of austenite–ferrite interface, Corros. Sci. 202 (2022) 110332.
[42] M.C. Young, S.L.I. Chan, L.W. Tsay, C.-S. Shin, Hydrogen-enhanced cracking of 2205 duplex stainless steel welds, Mater. Chem. Phys. 91 (1) (2005) 21–27.
[43] M.Y. Maeda, M. Koyama, H. Nishimura, O.M. Cintho, E. Akiyama, Hydrogen-assisted damage evolution in nitrogen-doped duplex stainless steel, Int. J. Hydrogen Energy. 46 (2) (2021) 2716–2728.